The Astrophysical Journal, 622:1225–1239, 2005 April 1
© 2005. The American Astronomical Society. All rights reserved. Printed in U.S.A.

CORONAL MASS EJECTION SHOCK AND SHEATH STRUCTURES RELEVANT TO PARTICLE ACCELERATION

W. B. Manchester IV, T. I. Gombosi, D. L. De Zeeuw, I. V. Sokolov, I. I. Roussev, and K. G. Powell
Center for Space Environment Modeling, 2455 Hayward Street, University of Michigan, Ann Arbor, MI 48109

J. Kóta
Lunar and Planetary Laboratory, 1629 East University Boulevard, University of Arizona, Tucson, AZ 85721

G. Tóth
Center for Space Environment Modeling, 2455 Hayward Street, University of Michigan, Ann Arbor, MI 48108;
and Department of Atomic Physics, Eotvos University, Budapest, Hungary

and

T. H. Zurbuchen
University of Michigan, 501 East University Avenue, Ann Arbor, MI 48108
Received 2004 June 23; accepted 2004 November 22

ABSTRACT

Most high-energy solar energetic particles are believed to be accelerated at shock waves driven by coronal mass ejections (CMEs). The acceleration process strongly depends on the shock geometry and the structure of the sheath that forms behind the shock. In an effort to understand the structure and time evolution of such CME-driven shocks and their relevance to particle acceleration, we investigate the interaction of a fast CME with the ambient solar wind by means of a three-dimensional numerical ideal MHD model. Our global steady state coronal model possesses high-latitude coronal holes and a helmet streamer structure with a current sheet near the equator, reminiscent of near solar minimum conditions. Fast and slow solar winds flow at high and low latitude, respectively, and the Archimedean spiral geometry of the interplanetary magnetic field is reproduced by solar rotation. Within this model system, we drive a CME to erupt by introducing a Gibson-Low magnetic flux rope that is embedded in the helmet streamer in an initial state of force imbalance. The flux rope rapidly expands and is ejected from the corona with maximum speeds in excess of 1000 km s^{-1}, driving a fast-mode shock from the inner corona to a distance of 1 AU. We find that the ambient solar wind structure strongly affects the evolution of the CME-driven shocks, causing deviations of the fast-mode shocks from their expected global configuration. These deflections lead to substantial compressions of the plasma and magnetic field in their associated sheath region. The sudden postshock increase in magnetic field strength on low-latitude field lines is found to be effective for accelerating particles to the GeV range.

Subject headings: acceleration of particles — MHD — shock waves — Sun: coronal mass ejections (CMEs)

1. INTRODUCTION

Coronal mass ejections (CMEs), in which large-scale expulsions of plasma are seen as bright arcs in coronagraph images, are the most stunning activities of the solar corona. Typically 10^{15}–10^{16} g of plasma is hurled into interplanetary space with a kinetic energy of order 10^{31}–10^{32} ergs. Because of their energetics and global scale, CMEs are of interest because of the large disturbances they produce and because they are associated with a restructuring of the solar corona (Low 2001). CMEs range in speed from 20 to 2500 km s^{-1}. CMEs with speeds in excess of the ambient solar wind (fast CMEs) eventually drive shocks ahead of them as they propagate from the Sun. For several CMEs, clear signatures of shock formation in the corona have been observed. As an example, Sime & Hundhausen (1987) observed a bright loop at the front of a CME that they identified as a coronal shock on the basis of the high speed of the loop (1070 km s^{-1}), the absence of any deflections preceding the CME, and that the expanding loop did not cease its lateral motion to form stationary legs. More recently, Raymond et al. (2000) and Mancuso et al. (2002) reported shocks traveling at more than 1000 km s^{-1} in the low corona ($r < 3\ R_{\odot}$) that were simultaneously observed with the Ultraviolet Coronagraph Spectrometer (UVCS) and as type II radio bursts. UVCS gave clear spectroscopic evidence for velocity and temperature changes at shock fronts, while radio bursts indicated the presence of shock-accelerated electrons.

Most energetic particles observed near Earth occur in so-called gradual events, lasting for several hours or days (Reames 1999). They are in clear contrast to impulsive particle events, which are observed to be more bursty and associated with flares. Gradual events are accelerated by CME-driven shocks as they propagate from the low corona throughout the heliosphere. Gradual events are of critical importance for space weather (Reames 1999). The acceleration of energetic particles at CME-driven shocks is therefore at the center of interest of models designed to predict space weather. However, the coupling between the complexity of CMEs described in MHD simulations and particle acceleration and transport is complex, and a number of simplifying assumptions have been used. Recent time-dependent calculations of shock-driven solar energetic particle (SEP) acceleration have relied on spherically symmetric shock propagation models that do not include CME initiation or interaction of the shock with a structured solar wind (Zank et al. 2000; Li et al. 2003; Lario 1998). Currently there are several existing CME models (e.g., Forbes & Priest 1995; Gibson & Low 1998, hereafter GL98; Wu et al. 1999; Antiochos et al. 1999; Amari et al. 2000; Riley et al. 2002; Manchester 2003; Roussev et al. 2004; Manchester et al. 2004a), some of which (e.g., Wu et al. 1999; Riley et al. 2002; Roussev et al. 2004; Manchester et al. 2004a) are global models that

include a solar wind and hence can address shock formation and propagation. In particular, models by Manchester et al. (2004a) and Roussev et al. (2004) describe fast CMEs driving shocks in the low corona ($r < 3\,R_\odot$). Roussev et al. (2004) simulated the passage of a CME-driven shock through a coronal model on the basis of synoptic magnetic field observations of Carrington rotation 1935. Roussev et al. (2004) then analyzed the shock and found that it was capable of accelerating protons to energies of 1 GeV. More recently, Sokolov et al. (2004) have calculated the time-dependent energy spectrum of particles accelerated at the shock produced in the model of Roussev et al. (2004).

The propagation of disturbances from the inner corona to 1 AU has been numerically modeled for many years now (e.g., Han et al. 1982a, 1988; Usmanov & Dryer 1995). More recent models have shown increasing degrees of sophistication, including magnetically driven eruptions that more closely resemble CMEs, as well as structured solar winds (e.g., Wu et al. 1999; Groth et al. 2000; Riley et al. 2002; Odstrcil et al. 2002; Manchester et al. 2004b). Here we examine the model of Manchester et al. (2004b) and analyze the structure of the CME-driven shock and its interaction with the solar wind. This numerical MHD model describes a CME driven by a three-dimensional magnetic flux rope propagating from the low corona, where the highest energy particles are accelerated all the way to 1 AU. The CME travels through an ambient solar wind that is representative of a solar minimum configuration. Our work follows studies by Odstrcil & Pizzo (1999) that simulated the interaction of CMEs with the solar wind. Here we explore in detail how the CME-driven shock is deformed by the bimodal solar wind and show a number of surprising results. For example, we find near-ecliptic postshock compressions that are comparable to those found at the shock, along with large increases in magnetic field strengths behind parallel shocks.

As described in Manchester et al. (2004a), the CME propagation starts with a system that is initially out of equilibrium and follows the resulting time evolution. The steady state corona and bimodal solar wind are based on the model of Groth et al. (2000), which includes open polar field lines and low-latitude closed field lines forming a streamer belt. Within this system, a (three dimensional) magnetic flux rope (taken from a family of analytical solutions of GL98) is placed within the streamer belt with both ends tied to the inner boundary. The application of a flux rope to the streamer belt follows from the belief that CMEs originate from coronal streamers (Hundhausen 1987, 1993). In our model, we find that the rapidly expanding flux rope drives a strong fast-mode shock ahead of it as the rope is expelled from the corona and travels to 1 AU. It is important to note that the results described here should not strongly depend on the details of the CME initiation model, since they focus on the interaction of the CME with large-scale heliospheric structures ahead of the CME. We therefore believe that our results are valid far beyond the GL98 model used here for reasons of simplicity.

The organization of the paper is as follows. We give a brief description of the conservative form of the equations of MHD and the scheme used to solve them in § 2. Details of the steady state corona and solar wind are given in § 3, while an outline of the GL98 flux rope is given in § 4. Results of the CME simulation are given in § 5, which includes a discussion of shock structure and Mach number. Finally, in § 6, we discuss the simulation results and demonstrate the implications of the CME model for high-energy particle acceleration.

2. GOVERNING EQUATIONS OF THE MHD MODEL

In our model of the corona and heliosphere, we assume that the systems are composed of magnetized plasmas that behave as an ideal gas with the polytropic index $\gamma = 5/3$. The plasma is assumed to have infinite electrical conductivity so that the magnetic field is "frozen" into the plasma. Gravitational forces on the plasma are included, but only those forces due to the Sun; there is no self-gravitation of the plasma. Finally, volumetric heating of the plasma of a chosen form is assumed to occur in the corona. With these assumptions, the evolution of the system may be modeled by the ideal MHD equations, written in conservative form as

$$\frac{\partial \rho}{\partial t} + \nabla \cdot (\rho \boldsymbol{u}) = 0, \tag{1}$$

$$\frac{\partial (\rho \boldsymbol{u})}{\partial t} + \nabla \cdot \left[\rho \boldsymbol{u}\,\boldsymbol{u} + \left(p + \frac{B^2}{8\pi} \right) I - \frac{\boldsymbol{B}\,\boldsymbol{B}}{4\pi} \right] = \rho \boldsymbol{g}, \tag{2}$$

$$\frac{\partial \boldsymbol{B}}{\partial t} + \nabla \cdot (\boldsymbol{u}\,\boldsymbol{B} - \boldsymbol{B}\,\boldsymbol{u}) = 0, \tag{3}$$

$$\frac{\partial \varepsilon}{\partial t} + \nabla \cdot \left[\boldsymbol{u} \left(\varepsilon + p + \frac{B^2}{8\pi} \right) - \frac{(\boldsymbol{u}\,\boldsymbol{B})\boldsymbol{B}}{4\pi} \right] = \rho \boldsymbol{g}\,\boldsymbol{u} + (\gamma - 1) Q, \tag{4}$$

where ρ is the plasma mass density, $\boldsymbol{u}$ is the plasma velocity, $\boldsymbol{B}$ is the magnetic field, and p is the plasma pressure (sum of the electron and ion pressures). The volumetric heating term Q parameterizes the effects of coronal heating, as well as heat conduction and radiation transfer (see § 3). The gravitational acceleration is defined as $\boldsymbol{g} = -g(\boldsymbol{r}/r)\,(R_\odot/r)^2$, where $R_\odot$ is the solar radius and g is the gravitational acceleration at the solar surface. The total energy density ε is given by

$$\varepsilon = \frac{\rho u^2}{2} + \frac{p}{\gamma - 1} + \frac{B^2}{8\pi}, \tag{5}$$

where gravity is omitted from the energy equation since it is treated as a momentum source term. This system of eight equations describes the transport of mass, momentum, and energy, with three equations describing the evolution of the magnetic field given by Faraday's Law if we assume infinite electrical conductivity. These equations are then put in dimensionless form, using values of the density and ion-acoustic wave speed from a suitable part of the physical domain (in this case, the low corona) in addition to a reference length scale (in this case, the solar radius). The dimensionless equations are then solved, using the block-adaptive tree solar wind Roe-type upwind scheme (BATS-R-US) code (Powell et al. 1999; Groth et al. 2000). This code is designed to run efficiently on massively parallel computers and solves the MHD equations by using block-adaptive mesh refinement (AMR). This feature of the grid allows for order-of-magnitude variations in numerical resolution within the computational domain. Such an adaptive grid is necessary to clearly resolve structures such as shocks and current sheets in the context of a global coronal model extending beyond 1 AU.

3. STEADY STATE MODEL OF THE SOLAR WIND

To simulate the time-dependent behavior of a CME propagating from the low corona through the solar wind, a representative MHD model of the steady state background solar wind is required. With such a model, the evolution of a CME is then formulated as a propagation problem with the initial condition of the corona and solar wind specified by the steady state solution.

In this section, we describe our steady state model of the corona and solar wind, which is designed to approximately reproduce conditions near solar minimum. The essential features of this model are (1) open magnetic field lines forming coronal holes at high latitude, (2) closed magnetic field lines forming a streamer belt near the Sun at low latitudes, and (3) reproduction of the bimodal nature of the solar wind with a fast wind over the poles and a slow wind at low latitudes. A thin current sheet forms at the tip of the streamer belt and separates oppositely directed magnetic flux originating from the two poles. The model is simplified by alignment of the magnetic axis with the z-axis, so the solution is axisymmetric. In addition, solar rotation is included since the domain extends to more than 300 solar radii, at which distance the azimuthal component of the Parker (1963) spiral is significant. While the magnetic field structure of this steady state solution is simple, more recent models incorporate synoptic magnetogram observations for more realistic magnetic field configurations (Roussev et al. 2003).

The corona is composed of high-temperature ($T > 10^6$ K), low-density ($\rho \approx 10^{-16}$ g cm^{-3}) plasma composed primarily of ionized hydrogen, which expands outward at supersonic speeds, forming the solar wind (Parker 1963). The steady state model of the corona and solar wind described here was first developed by Groth et al. (2000) and has since been modified as described in Manchester et al. (2004a, 2004b). The simulation is performed in the inertial frame with the magnetic axis aligned with the z-axis. Our model of the solar wind extends to 336 $R_\odot$ in the direction in which the CME propagates. The steady state numerical model assumes that the base of the corona is at the inner boundary and acts as a reservoir of hot plasma with an embedded magnetic field. The temperature of that plasma is taken to be 2.85×10^6 K with a plasma density of $\rho = 2.5\times10^{-16}$ g cm^{-3}. The intrinsic magnetic field at the solar surface, $\boldsymbol{B}_0$, may be written as a multipole expansion of the form

$$B_{0k} = 3\frac{M_i r_i}{r^4}\frac{r_k}{r} - \frac{M_k}{r^3} + 7\frac{Q_{ijl}r_i r_j r_l}{r^8}\frac{r_k}{r} - 3\frac{Q_{ijk}r_i r_j}{r^7}, \quad (6)$$

where M_i ($i = 1$, 2, and 3) are the components of the dipole moment vector and Q_{ijk} are the octopole moment tensor components for which the octopole is aligned with the z-axis (there is no quadrupole moment in this model). Repeated indices are summed from 1 to 3, where $r_1 = x$, $r_2 = y$, and $r_3 = z$. We have taken the dipole aligned with the z-axis so that $M_x = M_y = 0$ and $M_z = b_0$. The dipole and octopole moments are chosen such that the maximum field strength is 8.4 G at the poles and 2.2 G at the equator.

Volumetric heating of the model corona is introduced in a way that attempts to mimic the effects of energy absorption above the transition region, thermal conduction, and radiative losses, as well as to satisfy known constraints of coronal heating. The heating function has the form

$$Q = \rho q_0\left(T_0 - \gamma\frac{p}{\rho}\right)\exp\left(-\frac{(r-R_\odot)^2}{\sigma_0^2}\right), \quad (7)$$

where the target temperature T_0 is 5.0×10^6 K poleward from a critical angle $\theta_0(r)$, which defines the coronal hole boundary, while $T_0 = 2.85\times10^6$ K equatorward of $\theta_0(r)$ in the streamer belt. The heating function is defined with $q_0 = 10^6$ ergs g^{-1} s^{-1} K^{-1}, where $R_\odot$ is equal to the solar radius and r is the heliocentric radius. The function $\theta_0(r)$ is defined as follows: for the region 1 $R_\odot < r < 7$ $R_\odot$,

$$\sin^2\theta_0 = \sin^2 17.^\circ5 + \frac{(1 - \sin^2 17.^\circ5)(r - R_\odot)}{8}, \quad (8)$$

which is equal to 17.°5 at the solar surface and increases to a value of $\theta_0 = 61.^\circ5$ at $r = 7\,R_\odot$. Beyond this radius, θ_0 increases more slowly, as

$$\sin^2\theta_0 = \sin^2 61.^\circ5 + \frac{(1 - \sin^2 61.^\circ5)(r - 7R_\odot)}{40}, \quad (9)$$

reaching a value of $\theta_0 = 90^\circ$ at $r = 47\,R_\odot$, which is then held fixed at 90° for $r > 47\,R_\odot$. The heating scale height function is kept constant in the streamer belt with $\sigma_0(r,\ \theta) = 4.5$ and increases inside the coronal hole as

$$\sigma_0(r,\ \theta) = 4.5\left(2 - \frac{\sin^2\theta}{\sin^2\theta_0}\right), \quad (10)$$

which gives a scale height for the volumetric heating that varies from 4.5 $R_\odot$ near the equator to 9 $R_\odot$ at the poles. It is important to mention that this heating function was designed with several free parameters to reproduce the observed overall features of the fast and slow solar winds.

3.1. *Computational Mesh*

The computational domain for the simulation extends over the range defined by $-192\ R_\odot < x < 192\ R_\odot$, $-48\ R_\odot < y < 336\ R_\odot$, and $-192\ R_\odot < z < 192\ R_\odot$, with the Sun placed at the origin. The system is initially resolved, with 22,772 self-similar $6\times6\times6$ blocks containing a total of 4.9 million cells. The blocks are distributed in size over eight levels of refinement; each subsequent level of refinement uses cells half the size of the previous level (in each dimension). In this case, cells range in size from 1/32 to 4 $R_\odot$ and are spatially positioned to highly resolve the central body and the flux rope, as well as the heliospheric current sheet. The grid is refined every 100 iterations during the first 10 hr after CME initiation, with the frequency reduced to every 200 iterations thereafter. AMR criteria are chosen so that blocks close to a chosen radial line with large time variations in density are preferentially refined. In this way, the high-resolution mesh tracks the shock and sheath in a particular radial direction. We perform three runs, first focusing the refinement at low latitude in the location of line 1 as shown in Figure 1 and then focusing the refinement at higher latitude in the location of lines 3 and 4. Resolution along the shock is maintained at 1/32 $R_\odot$ to a distance of more than 40 $R_\odot$ from the Sun. As the shock approaches 1 AU, we gradually reduce the grid resolution to $\frac{1}{8}R_\odot$.

3.2. *Boundary Conditions*

We specify appropriate boundary conditions at the inner boundary (the spherical surface $r = 1\ R_\odot$) and the outer boundary (the outer surfaces of the rectangular domain) in the following way. Coronal boundary conditions are a function of heliospheric latitude. In the coronal holes poleward of θ_0, the following values are prescribed in ghost cells inside $r = 1\ R_\odot$: $\rho = 2.5\times10^{-16}$ g cm^{-3}, $p = 5.89\times10^{-2}$ dynes cm^{-2}, $\boldsymbol{u} = 0$, and $\boldsymbol{B} = \boldsymbol{B}_0$. These values are then allowed to interact with the solution inside our physical domain through the $r = 1\ R_\odot$ boundary by solving the Riemann problem at the boundary. The boundary is

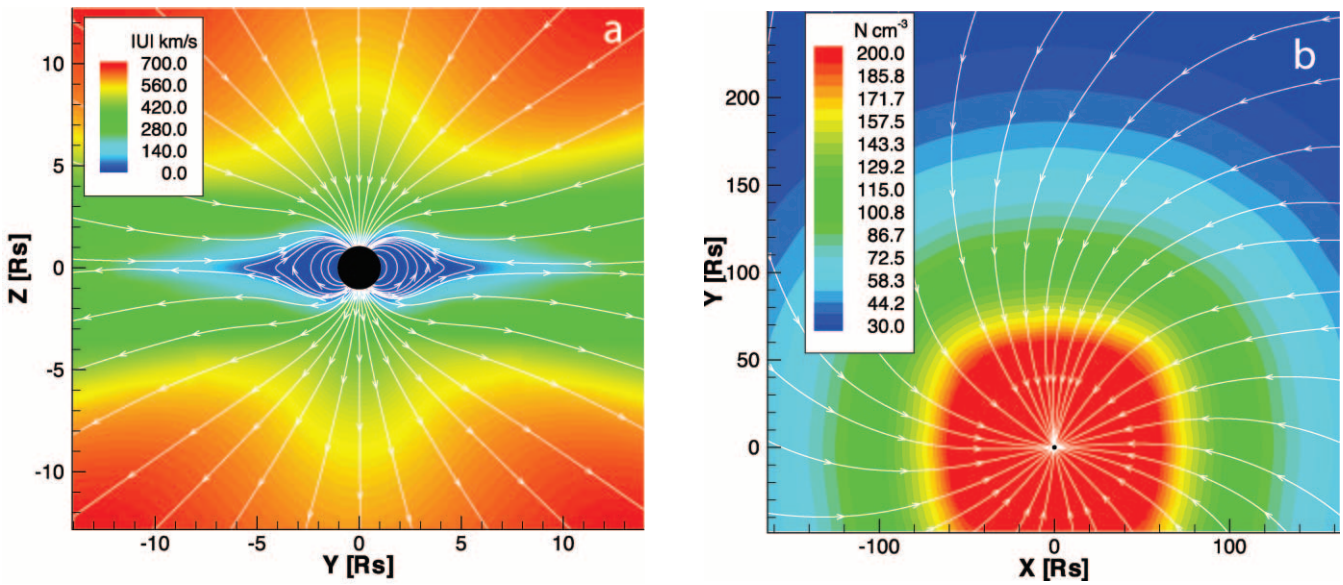

FIG. 1.—(*a*) Color image of the velocity magnitude of the steady state solar wind solution in the meridional (*y*-*z*) plane. Streamlines drawn in white illustrate the direction of the magnetic field in the plane. Note the bimodal nature of the solar wind speed. (*b*) Two-dimensional magnetic streamlines, showing the Parker spiral confined to the *x*-*y* plane located at $z = 25\ R_\odot$, which is superposed on a color image of the plasma density.

treated as a discontinuity in which the inside values are the prescribed boundary values and the outside values are taken from the adjacent active cell. The solution to the Riemann problem provides the fluxes of mass, energy, momentum, and magnetic field associated with the propagation of waves from the discontinuity. This approach ensures that the appropriate information from the "solar" values is propagated into the solution domain by the numerical flux function used in the scheme. These conditions set up a pressure gradient that drives plasma away from the Sun and permits the plasma to pass through the boundary as the mass source for the solar wind. The magnetic field at the surface is specified by the time-independent multipole expansion for the intrinsic field given by equation (6). In the streamer belt equatorward of θ_0, the following values are prescribed just inside $r = 1\ R_\odot$: $\partial\rho/\partial r = 0$, $\partial p/\partial r = 0$, $\boldsymbol{u} = -\boldsymbol{u}_{\rm out}$, and $\boldsymbol{B} = \boldsymbol{B}_{\rm out}$, where the subscript "out" refers to the values just outside $r = 1\ R_\odot$, which are computed by the flow solution scheme. These conditions strictly enforce a zero flow at the boundary, both in the radial and tangential directions, with the exception of solar rotational flow. The boundary conditions also enforce continuity of the magnetic field across the surface $r = 1\ R_\odot$. This provision allows the magnetic field of the flux rope (prescribed in the streamer belt) to pass through the interface where the footpoints are "line tied" to the rotating surface. At the outer boundary of the domain, the flow is superfast. Thus, all waves are exiting the domain, and no information from outside the domain propagates into the domain.

3.3. *Steady State Solar Wind Solution*

The solar wind solution is produced by the time evolution of the system subject to the described heating function, intrinsic magnetic field, and boundary conditions. Local time stepping is used to speed up convergence, achieving a nearly steady state solution after 146,000 iterations with AMR periodically applied to resolve the heliospheric current sheet. Figure 1 depicts two two-dimensional cuts through the three-dimensional steady state model. Figure 1*a* shows a meridional slice, and Figure 1*b* shows a slice near the equatorial plane. The color image in Figure 1*a* indicates the velocity magnitude, $|\boldsymbol{u}|$, of the plasma, while the magnetic field is represented by solid white lines. The magnetic field remains closed at low latitude, close to the Sun, forming a streamer belt. At high latitude, the magnetic field is carried out with the solar wind to achieve an open configuration. Closer to the equator, closed loops are drawn out and at a distance ($r > 3R_\odot$) collapse into a field-reversal layer. The resulting field configuration has a neutral line and a current sheet originating at the tip of the streamer belt similar to the numerical solution originally obtained by Pneuman & Kopp (1971). Figure 1*b* shows a color image of magnetic stream lines in white formed to a Parker spiral by rotation applied to the inner boundary. The color image shows a $1/r^2$ falloff in solar wind plasma density.

Inspection of Figure 1*a* reveals a bimodal outflow pattern with a slow wind, leaving the Sun below 400 km s^{-1} near the equator, and a high-speed wind above 750 km s^{-1}, found above 30° latitude. The variation in solar wind speed in this model results from the variation in latitude of coronal heating and open magnetic flux expansion. The variation in solar wind speed, as well as an increase in density near the heliospheric current sheet (the plasma sheet), is shown to have a profound influence on the shock structure and the associated particle acceleration. Note that this model is very simplified compared with the observed solar wind and follows earlier models of a bimodal solar wind, such as that of Wang et al. (1998). For example, the slow solar wind is likely time dependent, leading to large magnetic field deviations. In addition, fast and slow solar winds likely come from different sources, perhaps accelerated by entirely different heliospheric processes. These effects are currently not included in any three-dimensional Sun-heliosphere model. The omission of these effects should be expected to impact the large-scale structure of magnetic field lines in the corona, as well as the actual connectivity between the corona and the heliosphere.

4. FLUX ROPE OF GL98

The CME is initiated within this coronal model by superposing a three-dimensional GL98 magnetic flux rope on the streamer belt in an initial state of force imbalance, as we have previously

reported (Manchester et al. 2004a, 2004b). We briefly describe the mathematical form of the GL98 solutions, while more complete derivations and descriptions of the solutions can be found in the Appendix.

The solution for this flux rope is derived by applying the mathematical stretching transformation $r \rightarrow r - a$ to an axisymmetric, spherical ball of twisted magnetic flux in equilibrium with plasma pressure. The transformation, performed in spherical coordinates (r, θ, ϕ), draws space toward the origin while holding the angular coordinates, θ and ϕ, fixed. This mathematical procedure serves two important purposes. First, it generates a geometrically complex solution by distorting the originally spherical, axisymmetric flux rope (centered away from the heliocentric origin) into a teardrop shape with full three-dimensional spatial variation. The second benefit of the stretching transformation is the introduction of Lorentz forces associated with the magnetic field that requires both the pressure and weight of plasma in a $1/r^2$ gravitational field to be in static equilibrium. The density structure of the model has a dense helmet streamer containing a cavity embedded with a prominence-type density enhancement. Such long-lived coronal structures are often observed to give rise to CMEs (see Hundhausen 1993).

With our inclusion of the GL98 flux rope in a numerical steady state model of the corona and solar wind, we can allow the GL98 flux rope to interact self-consistently with a realistic structured solar wind. We determine to what degree a three-dimensional magnetic flux rope ejected from the low corona as a CME can evolve to drive shocks through the heliosphere. To begin, we do not ascribe a flow field to the flux rope and surrounding corona, but rather the CME results from an initial force imbalance due to the removal of part of the plasma in the flux rope. Substantial force imbalance, resulting from insufficient background coronal plasma pressure, offsets the magnetic pressure of the flux rope.

4.1. *Insertion of a Flux Rope*

For this simulation, the flux rope is specified by setting $a = 0.7$, $r_0 = 1.0$, $r_1 = 1.8$, and $a_1 = 0.93$ (see the Appendix). The flux rope and the contained plasma are linearly superposed on the existing corona so that the mass and magnetic field of the flux rope are added directly to the corona. The equilibrium state of GL98 requires a significant outwardly increasing plasma pressure to offset the magnetic pressure in the upper portion of the magnetic flux rope. The background corona is insufficient to provide this pressure, which leaves the flux rope with unbalanced magnetic forces that drive the eruption. We stress that the specific model used here does not address the CME initiation process, but this does not substantially affect our conclusions concerning CME propagation. The GL98 model allows for a numerically inexpensive generation of a fast CME whose interactions with the heliosphere are studied here.

5. SIMULATION OF THE CME EVENT

In this section, we present the results of a three-dimensional numerical simulation designed to study the evolution of a GL98 flux rope expanding from the corona that drives a shock front propagating to 1 AU. The simulation begins at $t = 0.0$ with the initiation of the CME, which evolves as the flux rope rapidly accelerates to speeds in excess of 1000 km s^{-1} and then begins to decelerate as shown in Figure 2. Since the CME is not directly driven, the energy for the eruption must come from the pre-event coronal initial state. The CME erupts with a maximum of 4.2×10^{31} ergs of kinetic energy, 8.5×10^{31} ergs of thermal energy, and 1.5×10^{30} ergs of gravitational energy. The total kinetic+thermal+gravitational energy increase is 1.27×10^{32} ergs, which is supplied directly from the magnetic energy of the flux rope, which is liberated as the flux rope expands. Much of the magnetic energy initially goes into thermal energy of the shock-heated plasma, which is then absorbed by the coronal heat sources, as described in Manchester et al. (2004b).

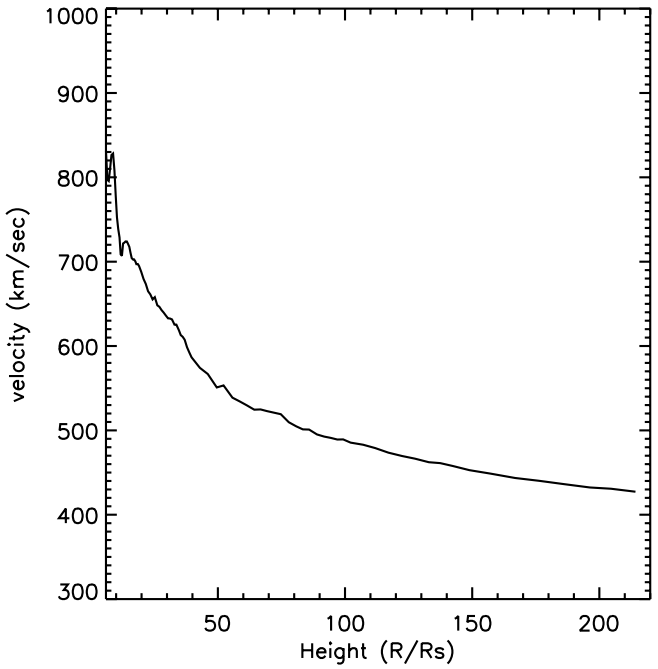

FIG. 2.—Radial velocity u_r of the front of the flux rope, plotted as a function of height along the y-axis.

A fast-mode MHD shock develops in the corona and propagates ahead of the flux rope to form a very extended shock front at 1 AU. The early evolution of the flux rope is nearly self-similar, but interaction with the solar wind quickly distorts the shock front, forming a dimple (a localized inward deformation), where the shock propagates slower at low latitude. Near the current sheet, a small dimple is expected to form because the characteristic propagation speed is slower where $\boldsymbol{B} = 0$, as seen in earlier simulations by Odstrcil et al. (1996) and Tsurutani et al. (2003). In addition to this effect, we find that the interaction of the shock with the bimodal solar wind results in a much larger and deeper indentation in the shock front, which extends well above the current sheet. This dimple has a profound effect on the postshock structure, as it results in the flow being deflected by the shock toward the equatorial plane, resulting in a significant postshock compression. Because of the compression, the plasma density and magnetic strength become significantly elevated beyond the levels achieved by the shock alone, which has profound implications for SEP acceleration. In a follow-up paper (Kóta et al. 2005), it is shown that this postshock compression may be more effective than the shock itself at energizing particles. Note that extensive use of AMR is essential to resolve the shock and CME sheath to clearly distinguish the shock and postshock compressions.

5.1. *The CME Morphology and Shock Propagation*

Two-dimensional views of the CME on the meridional y-z plane are presented at 1.5 and 10.0 hr in Figures 3*a* and 3*b*, respectively. The color images show the velocity magnitude for which a shock front is clearly visible preceding the flux rope. An indentation (outwardly concave dimple) forms in the shock

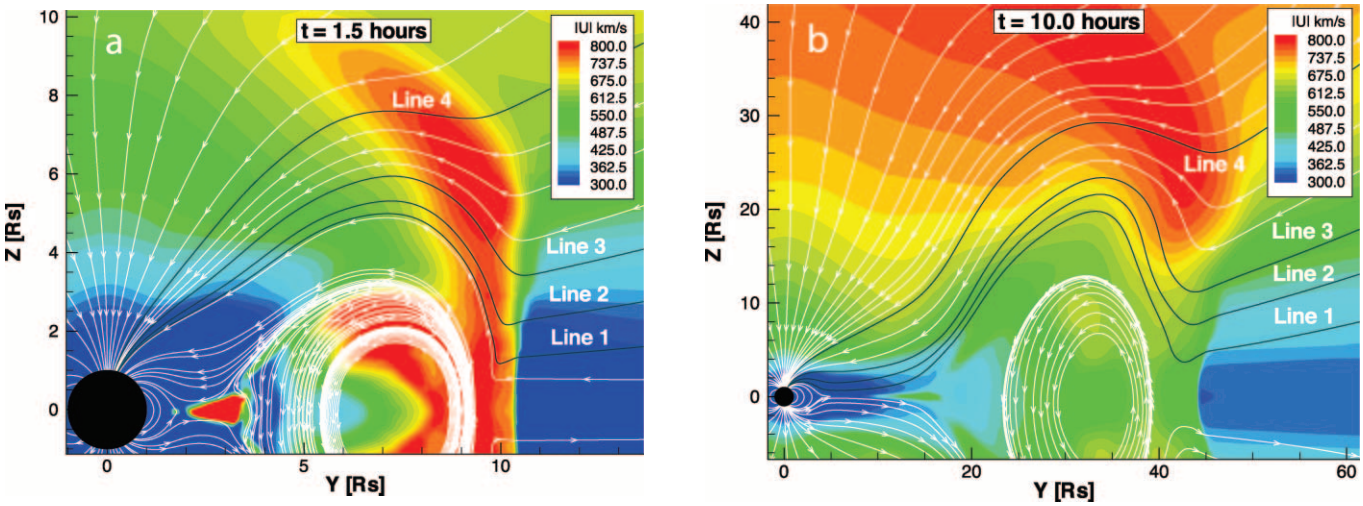

FIG. 3.—Color representations of the velocity magnitude on the *y*-*z* plane at (*a*) 1.5 and (*b*) 10.0 hr after CME initiation. Magnetic streamlines are drawn in white in both plots with the exception of four gray lines that are selected for close examination.

front as a result of the interaction of shock with the bimodal solar wind (Manchester et al. 2004a). At low latitude the shock propagates through the slow dense solar wind at a lower speed than it does through the fast streams found at high latitude. As a result, an indentation forms that deepens and broadens as the CME travels, as seen in Figure 3*b*. The magnetic field is illustrated by white and gray streamlines formed by integrating the B_y and B_z components and ignoring B_x. Consequently, the lines do not reflect the full three-dimensional structure of the magnetic field but show only its orientation confined to the *y*-*z* plane. The gray streamlines (labeled 1–4) have been chosen on the basis of their location along the shock front and are located at 7.°3, 12.°2, 17.°7, and 36.°7 heliospheric latitude, respectively. Lines 1, 2, and 3 pass through the indentation in the shock front, while line 4 passes through the wing of the shock front above the indentation.

Figure 4 shows four close-up views of the shock front on the meridional (*y*-*z* plane) at 1.5 hr. Magnetic streamlines are drawn in white, except lines 1–4, which are now colored magenta. Figures 4*a*, 4*c*, and 4*d* show color images of the azimuthal velocity, u_θ (where θ is measured from the equator), and Figure 4*b* shows a color image of the plasma density. The numerical mesh in all cases is shown in gray. Figures 4*a* and 4*b* show the numerical mesh resolved at the shock near line 1. We then repeated the simulation and resolved the mesh at the shock along lines 3 and 4 as shown in Figures 4*c* and 4*d*, respectively.

Because of the high speed of the shock relative to the ambient wind, the leading front is everywhere a fast-mode shock, which must deflect the field lines away from the shock normal. Given the orientation of the shock front, we thus expect that field lines in the dimple will be deflected toward the equator, while lines located in the wings of the shock will be deflected poleward. This behavior is in contrast to the outwardly concave slow-mode shock front found by Steinolfson & Hundhausen (1990), which deflects field lines poleward behind the dimple. Examining Figures 4*a* and 4*b*, we find that this is indeed the case, except for line 3, which appears to deflect across the shock normal as though it were an intermediate shock (e.g., De Sterck 1998). This apparent paradox is understood when we increase the numerical resolution at line 3 by a factor of 8 as shown in Figure 4*c* and then find that line 3 deflects toward the equator at the shock. Hence, field lines in the shock dimple must undergo two sharp transitions. First, they must pass through the shock to bend toward the equator, and then they must bend poleward in the sheath to wrap around the impinging flux rope. In contrast, field lines outside the dimple deflect away from the flux rope at the shock and then gradually bend around the flux rope in the sheath. What we see with line 3 in Figure 4*b* is that with poor numerical resolution the shock and postshock deflection of the field line blend together and cannot be distinguished, so as to be misleading about the nature of the shock.

Examining Figure 4, we find, not surprisingly, that the azimuthal velocity follows the same trend as the magnetic field. In the dimple, the flow is deflected poleward at the shock and then in the sheath abruptly reverses direction to move around the flux rope. The magnitude of the azimuthal flow is ± 100 km s^{-1}, and it reverses direction over a distance of approximately 2 numerical cell widths, as seen in Figure 4*a*. With the finer meshes, the flow reversal distance drops to 0.1 $R_\odot$, and the magnitude of the flow increases, resulting in larger velocity shears in the sheath. Such shear flows are susceptible to Kelvin-Helmholtz instabilities that could lead to turbulence behind the shock that would enhance particle diffusion and consequently particle acceleration. At higher latitude, the azimuthal flow makes a smooth transition to a positive velocity over a much larger distance. At high latitude, the equatorward flow in the ambient solar wind is a result of the expansion of the open magnetic flux in the solar wind as found by Suess et al. (1977). Finally, examining the structure of the density shown in Figure 4*a*, we find that near the center of the dimple the density increases by more than factor of 2 in the sheath. The density enhancement falls off with height, so that by line 3 there is very little increase beyond the shocked value.

At 10 hr, the flux rope front is at 40 $R_\odot$, and the standoff distance of the shock is 4.3 $R_\odot$ (at $z = 0$). The shock front moves steadily ahead of the rope, and the standoff distance is nearly proportional to the size of the flux rope and hence, to the distance from the Sun. The shock then reaches 1 AU (near the current sheet) at 69 hr, 16 $R_\odot$ ahead of the flux rope. The shock front extends much farther beyond the rope laterally, reaching the top of the computational domain $z = 192$ $R_\odot$ (latitude 57°) by 46 hr, while the flux rope extends only to $z = 46$ $R_\odot$. At this same time, the shock front extends in the equatorial plane to $x = 116$ $R_\odot$, corresponding to an angle of 66° from the *y*-axis.

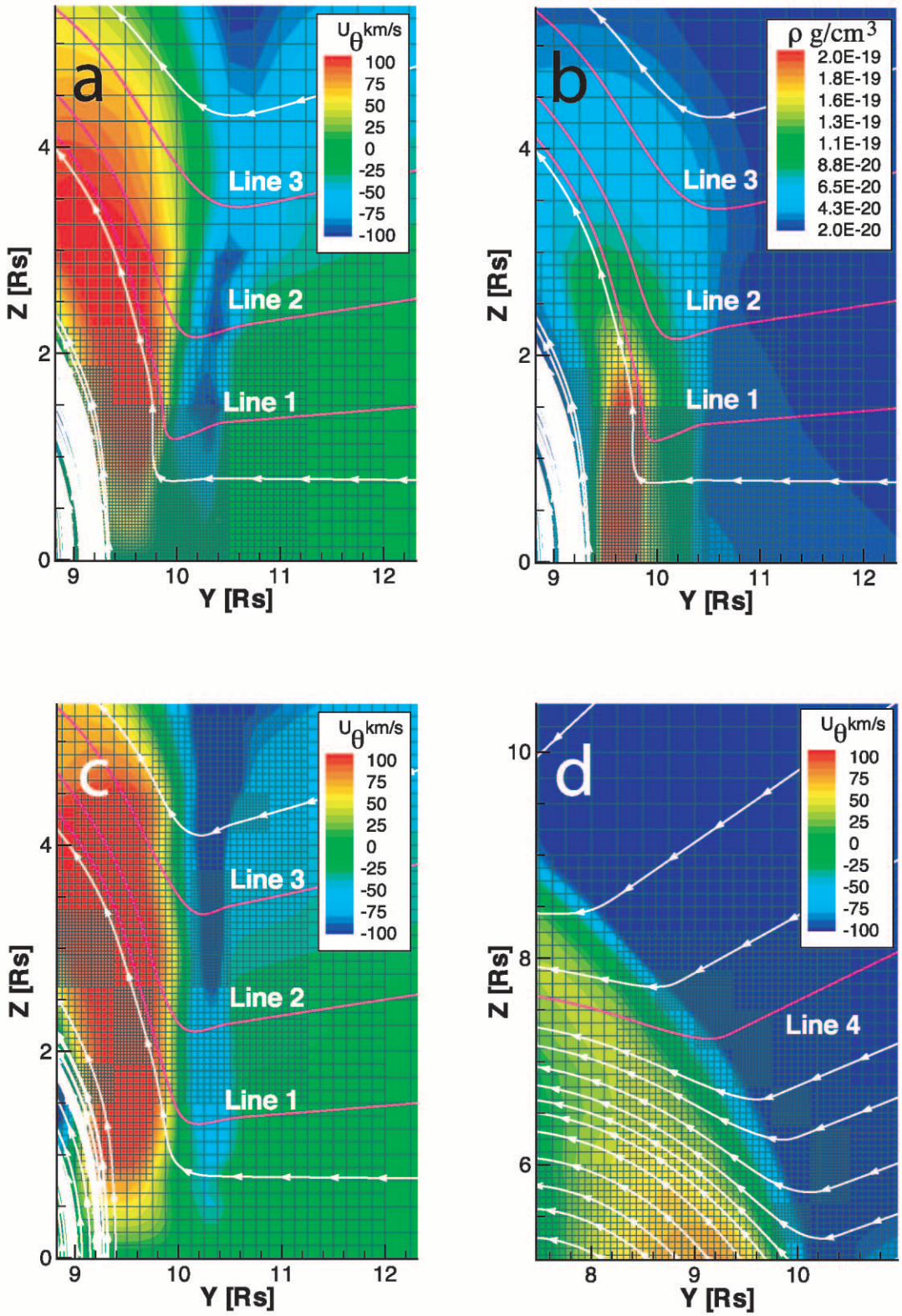

FIG. 4.—State of the system on the *y*-*z* plane at 1.5 hr. (*a*, *c*, *d*) Color images of the nonradial velocity (U_θ). (*b*) Image of the mass density. In all cases, magnetic streamlines are shown in white and magenta, while the computational mesh is shown in gray. The results of a simulation are shown in (*a*, *b*), in which the adaptive mesh highly resolves line 1 at the shock front. In contrast, the adaptive mesh is focused on lines 3 and 4 in (*c*, *d*), respectively. Note that in the cases in which the lines are resolved, field lines 1–3 bend toward the equator at the shock front, while only line 4 bends poleward to deflect away from the flux rope.

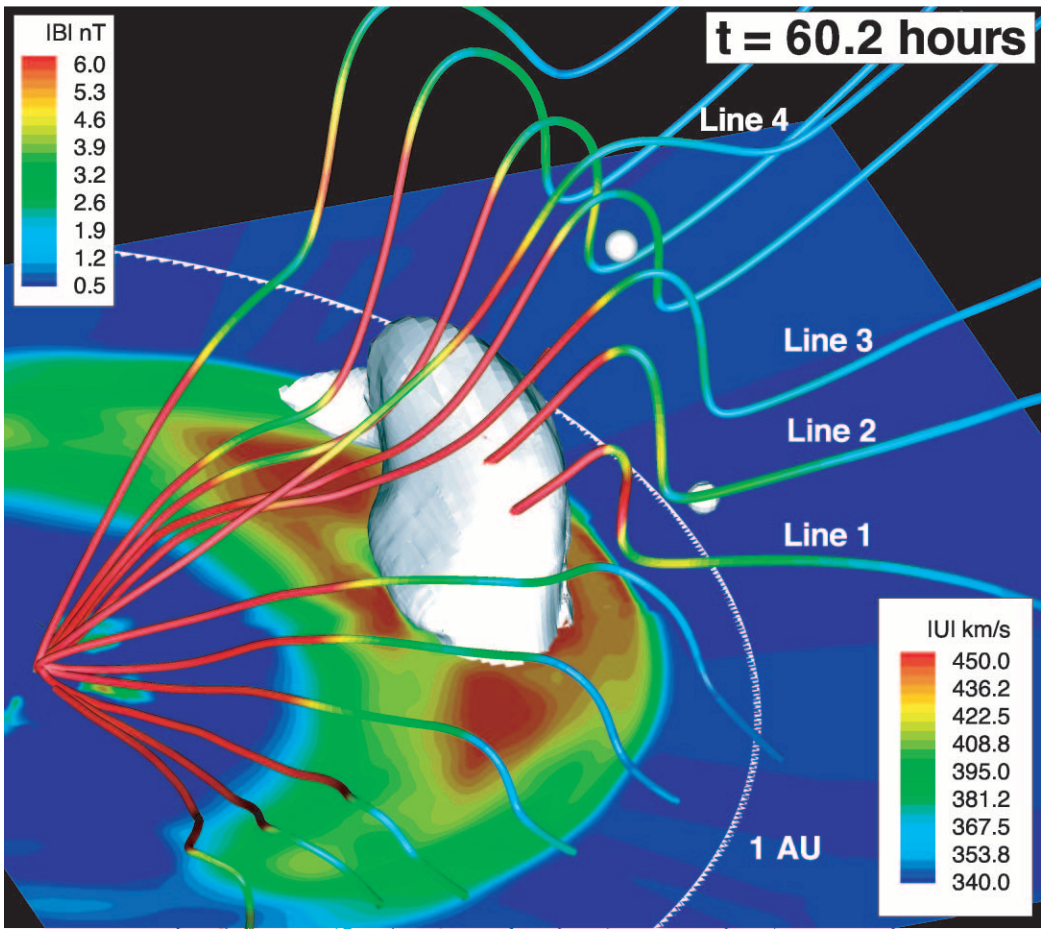

FIG. 5.—Three-dimensional representation of the heliospheric system as the CME approaches 1 AU at $t = 60.2$ hr. The flux rope is shown by an isosurface of magnetic field strength at 28 nT, while the velocity magnitude is shown in color on the equatorial (x-y) plane. Open magnetic field lines are shown in color to illustrate the magnetic field strength. The large spatial extent of the shock front is illustrated by the velocity on the plane, as well as the high latitude deformation of the field lines. Shaded spheres are placed at 1 AU to give perspective.

The large-scale shock front traveling through the solar wind at 60.2 hr is clearly seen in Figure 5, which displays a color representation of the velocity magnitude on the equatorial x-y plane. Protruding above this plane is an isosurface of magnetic field strength of 28 nT, which gives a three-dimensional view of the magnetic cloud formed by the flux rope as it approaches 1 AU. The solar wind magnetic field is represented by colored lines, which show the Parker spiral distorted by the fast-mode shock. The field lines are in colors to represent the magnitude of the field strength on the lines.

The shock and the magnetic structure at 1 AU depend not only on the initial conditions of the corona but also on the dynamic interaction between the CME and the ambient solar wind. As the CME propagates, the indentation in the shock front broadens to extend well above the flux rope as it approaches 1 AU. This large-scale concave feature of the shock front has been noted in earlier works on CME propagation such as Odstrcil et al. (1996). Along with the indentation in the shock front at 1 AU, we continue to find the postshock compression as shown in Figure 6. Here we see a close-up of the three-dimensional system at 60.2 hr. As in Figure 5, the magnetic cloud is shown as an isosurface of field strength, and field lines 1, 2, and 3 are shown in three-dimensional geometry viewed in the x-direction. Figures 6*b* and 6*c* show the field lines colored to represent magnetic field strength and plasma density, respectively. Figure 6*a* shows the field lines in front of the y-z plane, which is colored to show the azimuthal velocity. Looking at Figure 6, we see that the flow is deflected toward the equator by the shock at low latitude and that the poleward azimuthal flow extends far above the flux rope. Here the magnitude of the azimuthal flow is less than half the value found at 10 $R_\odot$. Figure 6*b* shows increases in magnetic field strength in the CME sheath. The variation is most noticeable along field line 1, where the magnetic field strength increases from 2.6 to 4.2 nT at the shock and then increases further, to 6.0 nT, for which the magnetic field bends around the flux rope. In contrast, the density along the field lines increases at the shock but shows little increase in the sheath. It should be noted that previous models of CME propagation have found increases in field strength in the sheath where field lines drape around the magnetic cloud (e.g., Vandas et al. 1996), which is not related to the shape of the shock front. Vandas et al. (1996) also suggest that local depressions in magnetic field strength near a magnetic cloud would serve as traps for energetic particles.

5.2. *Detailed Shock Structure*

Here we analyze the time evolution of the CME-driven shock structure and describe features capable of accelerating SEPs as is discussed in greater detail by Kóta et al. (2005). We examine the time evolution of the four selected magnetic field lines (see Fig. 3) and MHD quantities along those lines as the shock propagates over them. To begin, we present a time series of line plots

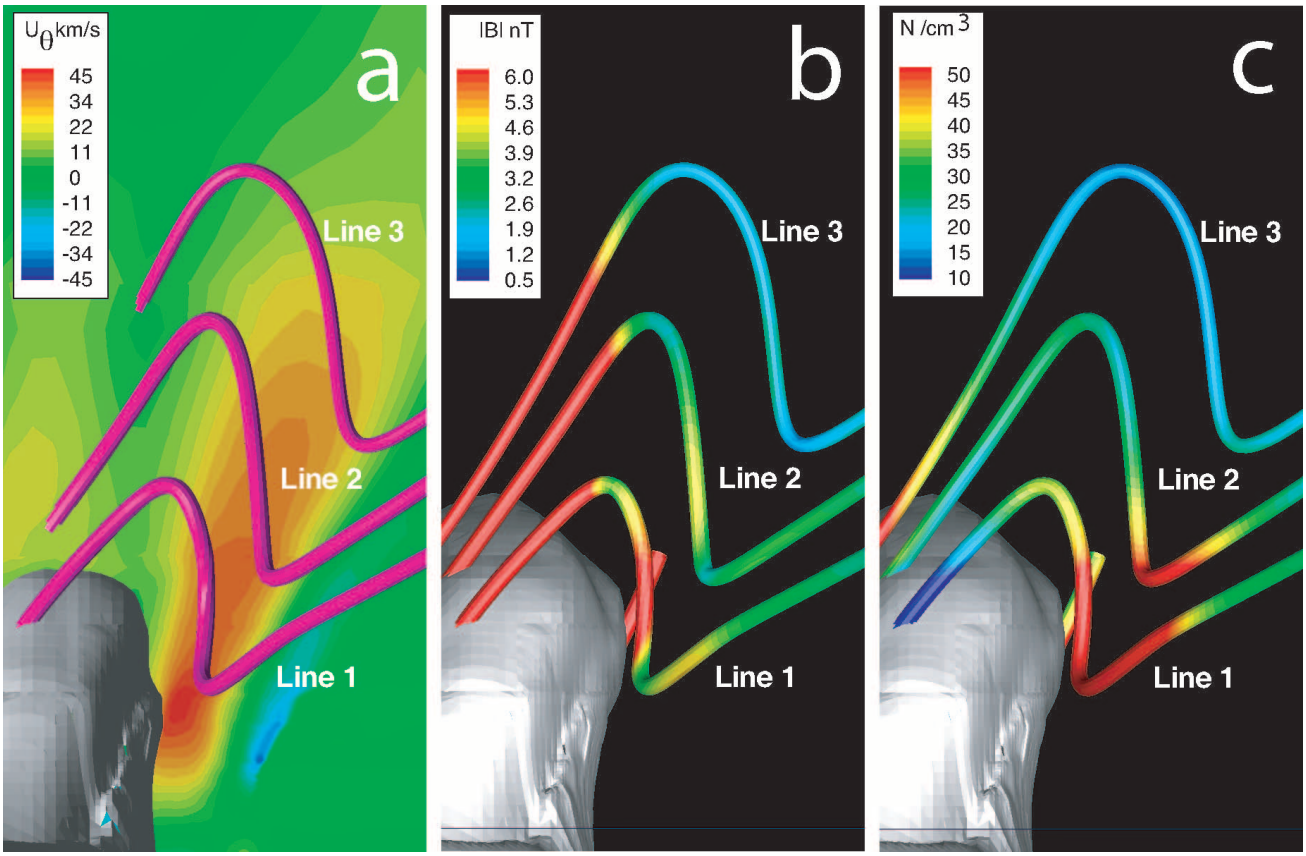

FIG. 6.—(*a*, *b*, *c*) Close-ups of magnetic field lines 1–3 and an isosurface of field strength (at 28 nT) at 60.2 hr. (*a*) Nonradial velocity (U_θ), shown on the *y*-*z* plane behind the lines; (*b*, *c*) field strength and density depicted in color on the field lines. Note that the increase in density occurs at the shock front, while the increase in field strength occurs primarily behind the shock, where the lines are deflected around the flux rope.

showing the field line geometry, plasma density, and magnetic field strength given at 15 minute intervals between $t = 0.75$ and 3.00 hr in Figure 7. Field strength is plotted for lines 1, 2, 3, and 4 in Figures 7*a*, 7*c*, 7*e*, and 7*g*, respectively, whereas density is plotted in Figures 7*b*, 7*d*, 7*f*, and 7*h*, respectively. Examining Figure 7*a*, we note that departures from the steady state field strength on line 1 first come as a small increase at the shock followed by an increase, which is more than an order of magnitude larger. Looking at Figure 7*b*, we see that the density evolution follows a similar two-stage pattern, with two distinct peaks, which become closer together at earlier times and finally merge for $t <$ 1.25 hr. For field line 2, the two-stage increase in density and field strength persists, although it is more difficult to discern than for line 1. At higher latitudes, the increases in density and field strength diminish, and on field lines 3 and 4 we find only solitary increases in both quantities.

To understand more clearly what is taking place as the shock passes over the chosen field lines, we need to closely examine the spatial variations behind the shock. It is also of interest to follow the evolution of the shock out to 1 AU. To this end, in Figure 8 we zoom in on the area of interest and show plots for density, field strength, and line shape with green, red, and black lines, respectively. These MHD quantities are plotted for field line 1 at 1.5, 10.0, and 60.2 hr in Figures 8*a*, 8*b*, and 8*c*, respectively. Field line 2 is shown at the same times in Figures 8*d*, 8*e*, and 8*f*, followed by line 3 in Figures 8*g*, 8*h*, and 8*i*, and line 4 in Figures 8*j*, 8*k*, and 8*l*. In all plots of Figure 8 we mark the location of the onset of the shock with a vertical black line.

Examining Figure 8*a* we see that a small increase in field strength occurs at the nearly parallel shock that only slightly compresses the magnetic field while deflecting the line toward the equator. The large increase in field strength occurs only where the field bends abruptly poleward to wrap around the flux rope. The density behaves differently, first increasing by nearly a factor of 4 at the shock and then increasing continuously behind the shock to reach a peak value just after the field line bends upward (poleward). The evolution of the field strength and density reveals that the postshock compression is nearly radial, so it hardly affects the nearly parallel magnetic field while significantly increasing the density. The field lines and flow then move upward, and the plasma expands in the vertical direction (*z*) parallel to the field while continuing to compress in the radial direction perpendicular to the field. As a result, the density drops sharply even as the magnetic field strength increases. The field strength finally decreases where the line crests pass around the flux rope.

Looking at Figures 8*b* and 8*c*, we see that at successively later times the increase in field strength at the shock grows as the shock propagates along the Parker spiral, causing the field to grow ever more perpendicular to the shock normal. The postshock increase in field strength remains very prominent, but the postshock increase in density is nearly lost by 10.0 hr. This lack of density enhancement clearly appears related to the shape of the field line, which slopes gently around the flux rope at 10.0 hr compared with the sharp bends toward the vertical direction found at 1.5 hr and later at 60.2 hr.

The structure and evolution of the shock on lines 2 and 3 are essentially the same as those on line 1, with successive reductions in the size of the density and field strength jumps. The field strength enhancement behind the shock extends to high latitude, well above the magnetic cloud, but it decreases in magnitude

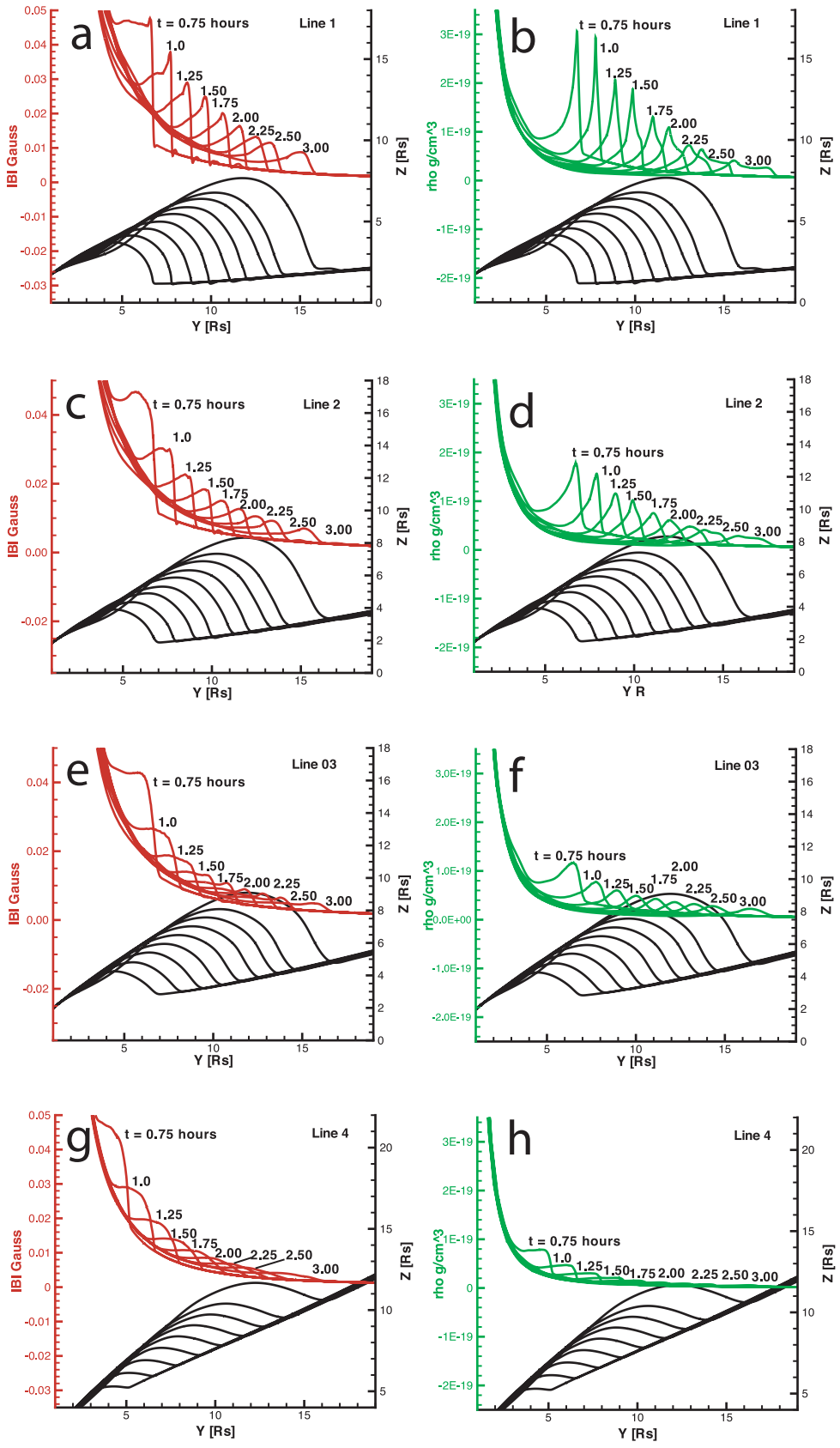

FIG. 7.—(*a*, *b*) Time series of plots depicting the evolution of the magnetic field strength (*red lines*) and density (*green lines*) along field line 1. Both plots show the geometry of field line 1 with a series of black lines at 0.75, 1.0, 1.25, 1.50, 1.75, 2.0, 2.25, 2.5 and 3.0 hr, corresponding to the density and field strength plots. (*c*, *d*), (*e*, *f*), and (*g*, *h*) Similar series of line plots for field lines 2, 3, and 4, respectively.

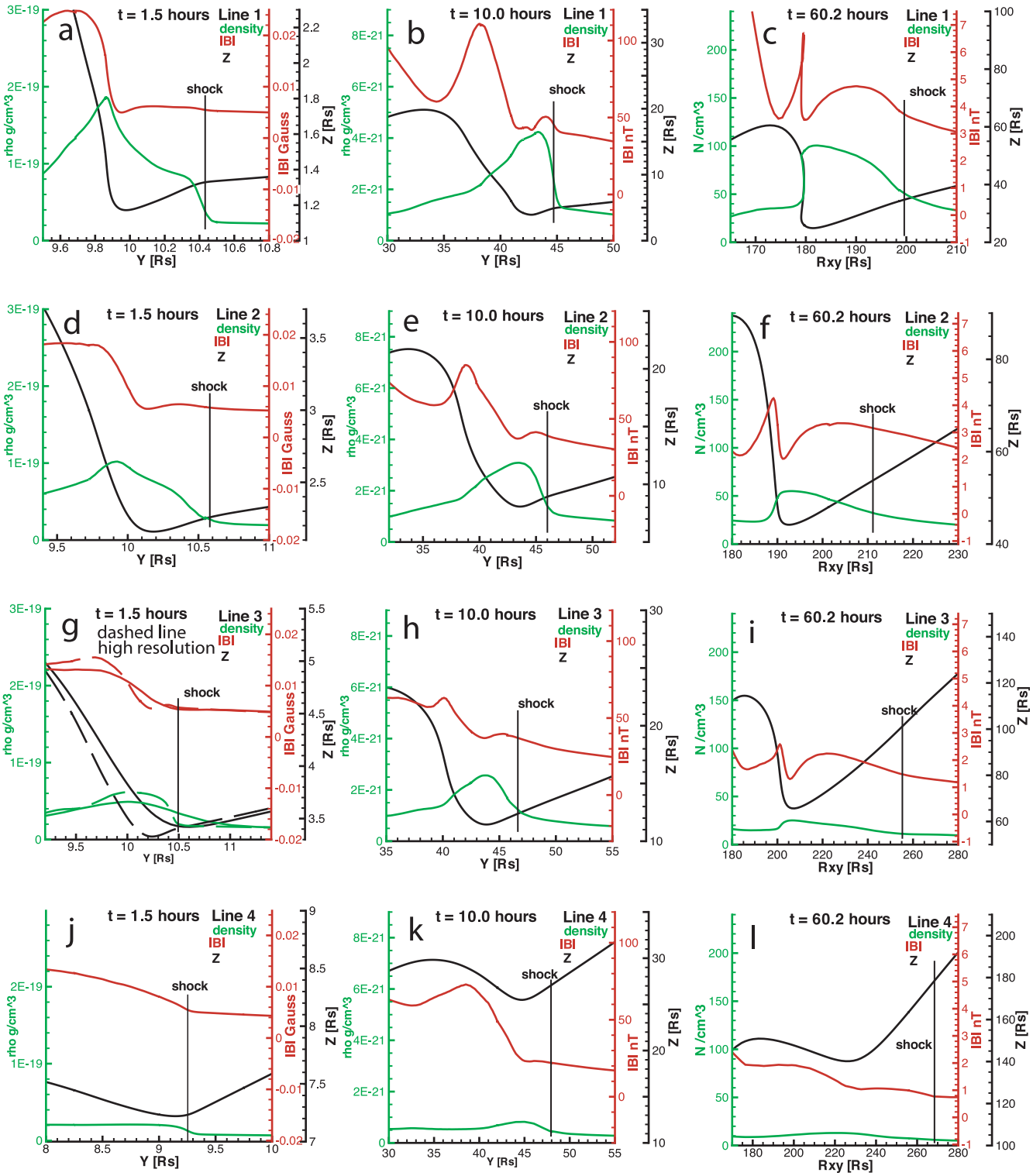

FIG. 8.—Shock structure on field lines 1–4 at 1.5 (*left column*), 10.0 (*middle column*), and 60.2 (*right column*) hr. Geometry of the four field lines is plotted with black lines, while field strength and mass density are plotted with red and green lines, respectively. (*a–c*) Line 1; (*d–f*) line 2; (*g–i*) line 3; (*j–l*) line 4; (*g*) low numerical resolution result (*solid lines*) and a high numerical resolution result (*dashed lines*). In all cases, there is significant postshock magnetic compression except for line 4 at 1.5 hr.

to be comparable to the increase at the shock. The structure seen on line 3 at 1.5 hr is exceptional in that it does not appear to exhibit a postshock increase in either quantity, as seen in Figure 7. However, with numerical resolution increased by a factor of 8 (Fig. 8*g*, *dashed lines*), we find that postshock increases in density and field strength are found, with the field line bending poleward clearly seen behind the shock. Finally, looking at line 4 at 1.5 hr with the same high resolution, we find that the field line deflects only at the shock. Close behind the shock, there is no increase in density and only a slow and modest increase in field

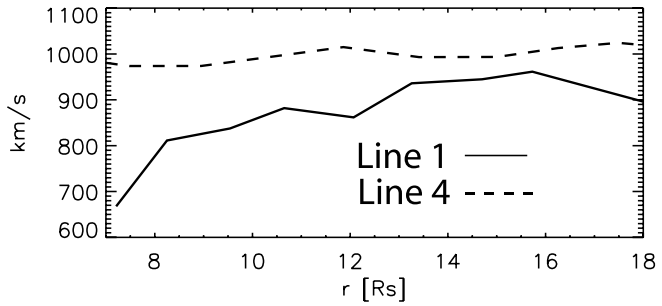

FIG. 9.—Fast-mode shock speed, plotted as a function of radial distance for field lines 1 (*solid lines*) and 4 (*dashed lines*).

strength. As the CME propagates, the indentation in the shock front broadens and envelopes line 4 by 10.0 hr, so that the postshock field line deflection occurs along with a postshock increase in field strength.

There is a clear difference in structure between the field lines in and outside the indentation in the shock front, which is seen most prominently with regard to lines 1 and 4. We now present an even more detailed analysis of the evolution of the shock along these field lines. To begin, we plot the shock speed along field lines 1 and 4 as a function of radial distance from the Sun in Figure 9. We note that the shock propagates at a higher, more uniform velocity near 1000 km s^{-1} on line 4 and that the shock accelerates to a lower velocity on line 1. Figure 10*a* shows the Mach number for the shocks plotted in solid lines, indicating that on line 4 the Mach number hovers around 2, while on line 1, the Mach number approaches 5. The wind and magnetosonic speeds are minimal in the heliospheric current sheet and both grow with heliospheric latitude. As a result, the shock travels in the high-latitude fast wind with a higher speed and lower Mach number than those found in the low-latitude slow wind (Manchester et al. 2004a). As the shock propagates farther out, the Mach number decreases as the shock decelerates. On line 1, the Mach number reaches values of 3.7 at 10 hr ($r = 46\ R_\odot$) and 1.8 at 60.2 hr ($r = 205\ R_\odot$). At these respective times on line 4, the Mach numbers are lower, at values of 1.5 ($r = 55\ R_\odot$) and 1.2 ($r = 294\ R_\odot$). Figure 10*a* (*dashed lines*) shows the angles between the field lines and the shock normals. Here we see that along line 4 the shock is initially nearly perpendicular to the magnetic field, as the shock basically broadsides the field line. As the shock expands and envelopes line 4, the angle drops to 10° by 20 $R_\odot$. In contrast, the shock remains nearly parallel to line 1 within 30 $R_\odot$. For both lines, the shock angles increase far from the Sun, reaching values near 45° at 1 AU because of the spiral nature of the magnetic field.

It is interesting to compare our findings with recent models of CME-driven shock formation. For example, Tsurutani et al. (2003) follow the propagation of a CME-driven shock from the low corona to 1 AU with an axisymmetric model that does not include a bimodal wind or spiral interplanetary magnetic field. We find that in both models the evolution of the shock normal (as measured from the *z*-axis) follows a similar pattern of remaining near 90° at low latitude and increasing at midlatitude as the shock front expands. In our model, the shock Mach number increases out to 18 $R_\odot$ and then decreases as the CME decelerates, whereas Tsurutani et al. (2003) find that the Mach number achieves a maximum at 130 $R_\odot$. Without a bimodal wind, Tsurutani et al. (2003) find only a small dimple in the shock front at the current sheet, and they find no evidence of postshock compression.

We next examine the evolution of jumps in the density and magnetic field strengths along the field lines. These quantities reflect the plasma and magnetic field compressions that are essential for particle acceleration through diffusive shock, first-order Fermi, and magnetic pumping (perpendicular acceleration), respectively. In Figure 10*b*, we plot the compression ratio of density and magnetic field strength at the locations of sudden increase along field lines 1 (*purple*) and 4 (*blue*). In this figure, density and

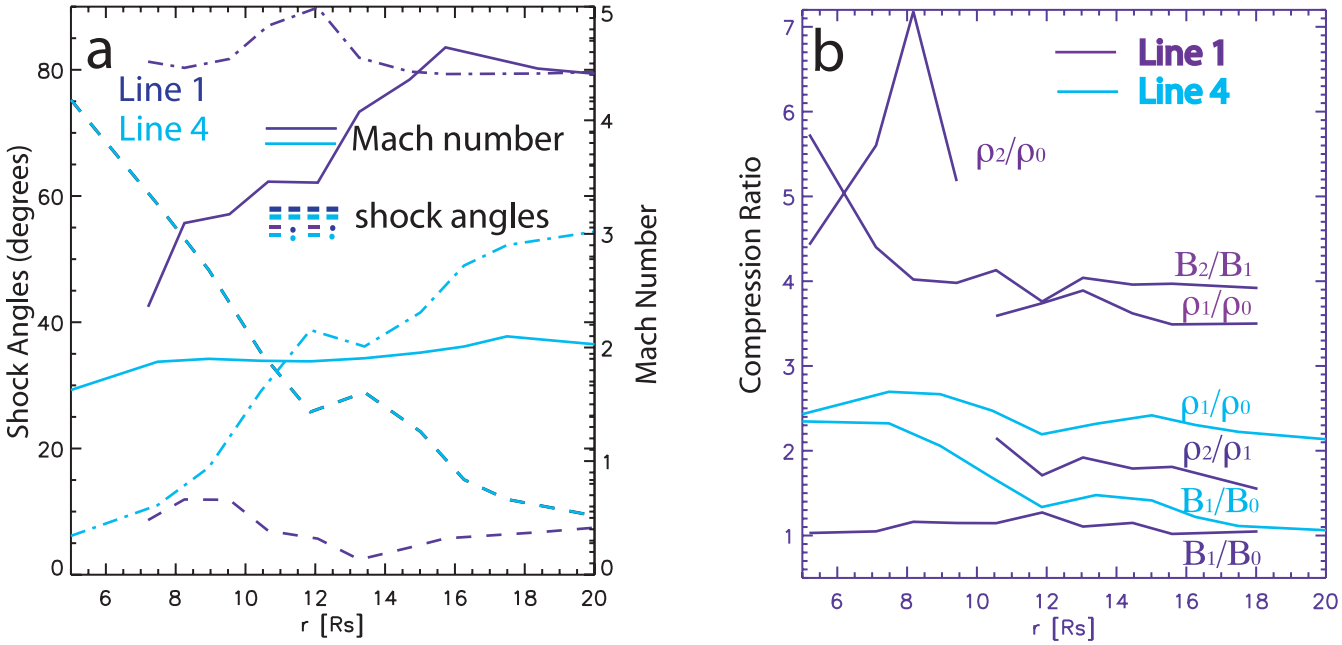

FIG. 10.—Time evolution of the fast-mode shock on lines 1 and 4. (*a*) Angle between the shock normal and magnetic field, plotted as a function of time with dashed lines for field lines 1 and 4. The angle between the shock normal and the *z*-axis on these field lines is plotted with dot-dashed lines, whereas solid lines show the evolution of the fast-mode Mach numbers. In all cases, lines plotted for field lines 1 and 4 are purple and light blue, respectively. (*b*) Shock compression ratio of the density (ρ_1/ρ_0) and magnetic field strength (B_1/B_0), plotted as functions of time for field lines 1 (*purple lines*) and 4 (*blue lines*). In addition, the postshock compression ratios for the density (ρ_2/ρ_1) and the magnetic field strength (B_2/B_1) are plotted for line 1. In the case for which the postshock density compression could not be distinguished from the shock compression, the total compression ratio (ρ_2/ρ_0) is plotted.

field strength jumps at shocks are labeled ρ_1/ρ_0 and B_1/B_0, respectively. Jumps behind the shock (in the sheath) are labeled ρ_2/ρ_1 and B_2/B_1, and in regions where the shock and postshock density compressions are unresolved, we label the jump ρ_2/ρ_0. We find that the increase in density at the shock on line 1 hovers close to the theoretical limit of 4 expected for a strong gasdynamic shock (Han et al. 1982b) with $\gamma = 5/3$, while the weaker shock on line 4 increases the density by no more than a factor of 2.7. In contrast, the magnetic compression at the shock on line 4 greatly exceeds that of line 1 close to the Sun because of the nearly perpendicular orientation of the shock on line 4. As the angle between the shock normal and the field decreases on line 4, so too does the magnetic compression, which falls from a value of 2.3 to little more than 1 for $r > 17\ R_\odot$.

Behind the indentation of the shock where field line 1 is located, we find postshock compression that increases the density and magnetic field over short length scales that are comparable to the shock width in our simulation. Examining Figure 10*b*, we find that the postshock density increase (ρ_2/ρ_1) is half that found in the shock. Magnetic field compression, however, is much larger in the sheath than it is at the nearly parallel shock and approaches a factor of 6 near the Sun. At distances less than $9\ R_\odot$ from the Sun the shock and postshock compression cannot be resolved, even with a grid cell size of $1/32\ R_\odot$. Here the compressions merge to form a single spike, for which the compression ratio exceeds 7. It must be pointed out that the density increase that occurs behind the shock close to the Sun is in part due to heat absorption from the sources that control coronal temperature. Where the temperature exceeds the coronal target temperature, which occurs behind the shock, the source terms absorb heat. For example, on line 1 at 1.5 hr the temperature drops from 10.7 million to 7.8 million K. Without this temperature drop, the density increases by only 25% rather than the 50%–100% found here. The heat absorption does not otherwise affect the sheath/shock structure, and far from the Sun the heat sources are negligible and have no impact on the structures shown at 10 and 60.2 hr.

6. DISCUSSION AND CONCLUSIONS

We have investigated the time evolution of a CME driven by a magnetic flux rope in an initial state of force imbalance. The CME model possesses observed characteristics of pre-event structures including a dense helmet streamer with a cavity and core threaded by a magnetic flux rope. The ambient solar wind has a bimodal velocity structure that is characteristic of conditions at solar minimum. The ensuing eruption originates in the low corona as the flux rope and entrained plasma expand into the solar wind with a peak speed in excess of 1000 km s^{-1}. We find that a fast-mode shock wave forms in front of the flux rope, which is distorted by its interaction with the bimodal solar wind, resulting in an indentation in the shock where it passes through the slow wind.

The increase in density and field strength at the shock front that accelerates particles are determined locally by the shock Mach number and orientation of the shock relative to the upstream magnetic field. However, the global shape of the shock front and upstream flow can also result in strong postshock compressions. In this case, we find that the indentation in the fast-mode shock front by the slow wind results in a flow converging toward the equatorial plane in front of the impinging flux rope. The flow must then suddenly reverse direction to move out of the way and pass around the rope. Here the flow is characterized by high-velocity shear and strong compression. Field lines in the shock indentation experience shock density compression exceeding that found at high latitude and a cumulative shock-sheath compression that together significantly exceed the maximum adiabatic shock compression. These same low-latitude field lines, while parallel to the shock normal, experience postshock increases in magnetic field strength that are more than twice as large as the shock increase of perpendicular shocks found at higher latitude.

We find that the interaction of a CME with a bimodal solar wind results in a structured shock and significant postshock compressions that cannot be realized by the spherically symmetric shock models that have been used to model particle acceleration (Zank et al. 2000; Li et al. 2003). We find that in these circumstances the large increases in the density and magnetic field strength found at low latitude behind the shock present a greater opportunity for particle acceleration than these spherical models suggest, as will be shown in greater detail by Kóta et al. (2005). We also find strong velocity shears behind the shock that could contribute to particle acceleration by increasing turbulence from the Kelvin-Helmholtz instability and hence increasing particle diffusion. Finally, we note that a large depression in magnetic field strength exists on low-latitude lines behind the sheath that extends out to 1 AU, as seen in Figure 8. Such a magnetic structure is significant in that suprathermal electrons in the magnetic depression are trapped, reflecting from the localized increases in field strength. In this case, there is the possibility of observing bistreaming electrons on open magnetic field lines that would give the impression of a closed structure in interplanetary space.

This simulation represents an ongoing effort to develop global space weather models that can track and resolve shocks to accurately derive MHD quantities from which SEP properties are calculated (Kóta et al. 2005). The success of our model in capturing many properties of CMEs, including properties of pre-event structures, a bimodal background solar wind, and shock formation, lead directly to conditions far more favorable for particle acceleration than has been recognized. With prescribed heating to drive the solar wind, we maintain $\gamma = 5/3$ through the entire computational domain. These thermodynamic properties allow us to better capture shocks with appropriate jump conditions compared with simpler models using reduced values of γ to drive the wind. Advanced AMR techniques have allowed us to track and resolve shocks and postshock structures that would otherwise be lost.

The simulations reported here were carried out on an Origin 3800 supercomputer at NASA Ames. The research for this manuscript was supported by Department of Defense MURI grant F49620-01-1-0359, NSF CISE grant ACI-9876943, NSF ITR grant 0325332, and NASA AISRP grant NAG5-9406 at the University of Michigan. G. Tóth is partially supported by the Education Ministry of Hungary (grant FKFP-0242-2000).

APPENDIX

MATHEMATICAL FORM OF THE GL98 FLUX ROPE

The flux rope is obtained by transforming a toroidal magnetic rope contained in a sphere of radius r_0. The center of the sphere is located at a radial distance of r_1 on the y-axis. The plasma pressure in the flux rope is proportional to the free parameter a_1^2, which also controls the magnetic field strength in the flux rope through pressure balance.

Mathematically, the flux rope magnetic field is written in terms of a scalar flux function A in spherical coordinates (r', θ', ϕ') as

$$\boldsymbol{b} = \frac{1}{r' \sin\theta'}\left(\frac{1}{r'}\frac{\partial A}{\partial \theta'}\hat{\boldsymbol{r}}' - \frac{\partial A}{\partial r'}\hat{\boldsymbol{\theta}}' + \alpha_0 A \hat{\boldsymbol{\phi}}'\right), \tag{A1}$$

where

$$A = \frac{4\pi a_1}{\alpha_0^2}\left[\frac{r_0^2}{g(\alpha_0 r_0)}g(\alpha_0 r') - r'^2\right]\sin^2\theta', \tag{A2}$$

$$g(\alpha_0 r') = \frac{\sin\alpha_0 r'}{\alpha_0 r'} - \cos\alpha_0 r'. \tag{A3}$$

The pressure inside the flux rope necessary for equilibrium is $\Pi = a_1 A$, where a_1 is a free parameter that determines the magnetic field strength and the plasma pressure in the flux rope. Here r_0 is the diameter of the spherical ball of flux and α_0 is related to r_0 by $\alpha_0 r_0 = 5.763459$ (this number is the smallest eigenvalue of the spherical Bessel function, $J_{5/2}$). The coordinate (r', θ', π') is centered relative to the heliospheric coordinate system on the y-axis at $y = r_1$ and oriented such that the circular axis of the flux rope is in the heliospheric equatorial plane.

In the next step, this axisymmetric flux rope is subjected to the mathematical transformation $r \rightarrow r - a$ (where a is the stretching length in the radial direction) that draws space toward the heliospheric origin and distorts the sphere containing the rope to a teardrop shape. Following this transformation, the magnetic field takes the form

$$B_r(r,\ \theta,\ \phi) = \left(\frac{\Lambda}{r}\right)^2 b_r(\Lambda,\ \theta,\ \phi), \tag{A4}$$

$$B_\theta(r,\ \theta,\ \phi) = \left(\frac{\Lambda}{r}\frac{d\Lambda}{dr}\right) b_\theta(\Lambda,\ \theta,\ \phi), \tag{A5}$$

$$B_\phi(r,\ \theta,\ \phi) = \left(\frac{\Lambda}{r}\frac{d\Lambda}{dr}\right) b_\phi(\Lambda,\ \theta,\ \phi), \tag{A6}$$

where $\Lambda = r + a$ and (r, θ, ϕ) are the heliospheric spherical coordinates. Equilibrium within this transformed state demands that the plasma pressure be of the form

$$p = \left(\frac{\Lambda}{r}\right)^2\left[1 - \left(\frac{\Lambda}{r}\right)^2\right]\frac{b_r^2}{8\pi} + \left(\frac{\Lambda}{r}\right)^2 \Pi \tag{A7}$$

and that the density be of the form

$$\rho = \frac{1}{F(r)}\left\{-\left(\frac{\Lambda}{r}\right)^2\left[1 - \left(\frac{\Lambda}{r}\right)^2\right]\frac{d}{d\Lambda}\left(\Pi + \frac{b^2}{8\pi}\right) + 2\Pi\frac{\Lambda a}{r^3} + \frac{\Lambda a}{4\pi r^3}\left[1 - 2\left(\frac{\Lambda}{r}\right)^2\right]b_r^2 + \left(\frac{\Lambda}{r}\right)^2\left(\frac{a^2}{r_2} + \frac{2a}{r}\right)\left(\frac{b_\theta^2 + b_\phi^2}{4\pi\Lambda}\right)\right\}, \tag{A8}$$

where $F(r) = GM/r^2$, G is the gravitational constant, and M is the solar mass.

REFERENCES

Amari, T., Luciani, J. F., Mikić, Z., & Linker, J. 2000, ApJ, 529, L49
Antiochos, S. K., DeVore, C. R., & Klimchuk, J. A. 1999, ApJ, 510, 485
De Sterck, H., Low, B. C., & Poedts, S. 1998, Phys. Plasmas, 5, 4015
Forbes, T. G., & Priest, E. R. 1995, ApJ, 446, 377
Gibson, S., & Low, B. C. 1998, ApJ, 493, 460 (GL98)
Groth, C. P. T., DeZeeuw, D. L., Gombosi, T. I., & Powell, K. G. 2000, J. Geophys. Res., 105(A11), 25053
Han, S. M., Wu, S. T., & Dryer, M. 1988, Comput. Fluids, 16, 81
Han, S. M., Wu, S. T., & Nakagawa, Y. 1982a, Comput. Fluids, 10, 127
———. 1982b, Comput. Fluids, 10, 159
Hundhausen, A. J. 1987, in Solar Wind Six, Vol. 2, ed. V. J. Pizzo, T. E. Holzer, & D. G. Sime (NCAR Tech. Note 306+Proc; Boulder: Natl. Cent. Atmos. Res.), 181
———. 1993, J. Geophys Res., 98(A8), 13177
Kóta, J., Manchester, W. B., IV, Gombosi, T. I., DeZeeuw, D. L., Sokolov, I. V., & Tóth, G. 2005, ApJ, submitted
Lario, D., Sanahuja, B., & Heras, A. M. 1998, ApJ, 509, 415
Li, G., Zank, G. P., & Rice, W. K. M. 2003, J. Geophys. Res., 108, 1082
Low, B. C. 2001, J. Geophys. Res., 106(A11), 25141
Manchester, W. B., IV. 2003, J. Geophys. Res., 108(A4), 1162
Manchester, W. B., IV, Gombosi, T. I., Roussev, I., DeZeeuw, D. L., Sokolov, I. V., Powell, K. G., Tóth, G., & Opher, M. 2004a, J. Geophys. Res., 109(01), 01102
Manchester, W. B., IV, Gombosi, T. I., Roussev, I., Ridley, A. J., DeZeeuw, D. L., Sokolov, I. V., Powell, K. G., & Tóth, G. 2004b, J. Geophys. Res., 109(A02), 107
Mancuso, S., Raymond, J. C., Kohl, J., Ko, Y.-K., Uzzo, M., & Wu, R. 2002, A&A, 383, 267
Odstrcil, D., Dryer, M., & Smith, Z. 1996, J. Geophys. Res., 101(A9), 19973
Odstrcil, D., Linker, J. A., Lionello, R., Mikić, Z., Riley, P., Pizzo, V. J., & Luhmann, J. G. 2002, J. Geophys. Res., 107(A12), 1493
Odstrcil, D., & Pizzo, V. J. 1999, J. Geophys. Res., 104(A1), 483
Parker, E. N. 1963, Interplanetary Dynamical Processes (New York: Wiley)
Pneuman, G. W., & Kopp, R. A. 1971, Sol. Phys., 18, 258
Powell, K. G., Roe, P. L., Linde, T. J., Gombosi, T. I., & DeZeeuw, D. L. 1999, J. Comput. Phys., 154, 284
Raymond, J. C., et al. 2000, Geophys. Res. Lett., 27(10), 1439
Reames, D. V. 1999, Space Sci. Rev., 90, 413

Riley, P., Linker, J. A., Mikić, Z., Odstrcil, D., Pizzo, V. J., & Webb, D. F. 2002, ApJ, 578, 972
Roussev, I. I., Sokolov, I. V., Forbes, T. G., Gombosi, T. I., Lee, M. A., & Sakai, J. I. 2004, ApJ, 605, L73
Roussev, I. I., et al. 2003, ApJ, 595, L57
Sime, D. G., & Hundhausen, A. J. 1987, J. Geophys Res., 92, 1049
Sokolov, I. V., Roussev, I. I., Forbes, T. G., Gombosi, T. I., Lee, M. A., & Sakai, J. I. 2004, ApJ, 616, L171
Steinolfson, R. S., & Hundhausen, A. J. 1990, J. Geophys. Res., 95, 15251
Suess, S. T., Richter, A. K., Winge, C. R., & Nerney, S. F. 1977, ApJ, 217, 296
Tsurutani, B., Wu, S. T., Zhang, T. X., & Dryer, M. 2003, A&A, 412, 293
Usmanov, A. V., & Dryer, M. 1995, Sol. Phys., 159, 347
Vandas, M., Fischer, S., Geranios, A., Dryer, M., Smith, Z., & Detman, T. 1996, J. Geophys. Res., 101(A10), 21589
Wang, A. H., Wu, S. T., Suess, S. T., & Poletto, G. 1998, J. Geophys. Res., 103, 1913
Wu, S. T., Guo, W. P., Michels, D. J., & Burlaga, L. F. 1999, J. Geophys. Res., 104(A7), 14789
Zank, G. P., Rice, W. K., & Wu, C. C. 2000, J. Geophys. Res., 105, 25079